



High toughness well conducting contact layers for solid oxide cell stacks by reactive oxidative bonding

Ritucci, I.; Talic, B.; Kiebach, R.; Frandsen, H. L.

Published in:
Journal of the European Ceramic Society

Link to article, DOI:
[10.1016/j.jeurceramsoc.2020.11.021](https://doi.org/10.1016/j.jeurceramsoc.2020.11.021)

Publication date:
2021

Document Version
Version created as part of publication process; publisher's layout; not normally made publicly available

[Link back to DTU Orbit](#)

Citation (APA):
Ritucci, I., Talic, B., Kiebach, R., & Frandsen, H. L. (2021). High toughness well conducting contact layers for solid oxide cell stacks by reactive oxidative bonding. *Journal of the European Ceramic Society*, 41(4), 2699-2708. <https://doi.org/10.1016/j.jeurceramsoc.2020.11.021>

General rights

Copyright and moral rights for the publications made accessible in the public portal are retained by the authors and/or other copyright owners and it is a condition of accessing publications that users recognise and abide by the legal requirements associated with these rights.

- Users may download and print one copy of any publication from the public portal for the purpose of private study or research.
- You may not further distribute the material or use it for any profit-making activity or commercial gain
- You may freely distribute the URL identifying the publication in the public portal

If you believe that this document breaches copyright please contact us providing details, and we will remove access to the work immediately and investigate your claim.



Contents lists available at ScienceDirect

Journal of the European Ceramic Society

journal homepage: www.elsevier.com/locate/jeurceramsoc

Original Article

High toughness well conducting contact layers for solid oxide cell stacks by reactive oxidative bonding

I. Ritucci*, B. Talic, R. Kiebach, H.L. Frandsen

Department of Energy Conversion and Storage, Technical University of Denmark, Roskilde, DK-4000, Denmark

ARTICLE INFO

Keywords:

Solid oxide cell
Fracture toughness
Interconnect
Contact layer
Coating

ABSTRACT

The increasing demand for large scale electrochemical conversion technologies, suppose a scale-up of the solid oxide cell (SOC) technologies. SOCs offer high conversion efficiency compared to competing technologies, but the brittleness of the ceramic components makes up-scaling a challenge, as these challenges grows with the size of the stack. Here, we present a new type of contact layer to be used between the oxygen electrode and the interconnect, which can be applied by a scalable, low-cost processing routes. The microstructural and compositional development of the contact layers was studied by X-ray diffraction and electron microscopy and the performance was evaluated by measuring the fracture toughness and area specific resistance. Five times higher toughness compared to conventional contact layers is achieved by reactive oxidative bonding at moderate temperatures. In this process metal particles (Cu, Co, Mn) are in-situ oxidized to well conductive spinels with low area specific resistance ($<23 \text{ m}\Omega\text{cm}^2$, $750 \text{ }^\circ\text{C}$).

1. Introduction

Solid oxide fuel cells (SOFC) are electrochemical devices that can convert fuels such as hydrogen, ammonia or hydrocarbons into electricity with a high efficiency [1–3]. When operated in reversed mode as a solid oxide electrolysis cell (SOEC), the same device can be used to produce hydrogen or syngas. These gasses can be stored or converted into higher value chemicals [4–7]. In order for the solid oxide cell (SOC) technology to reach commercialization, their long-term stability and reliability must be successfully demonstrated [8].

Establishing a robust contact between the oxygen electrode and the metallic interconnect is among the major durability challenges for state-of-the-art SOC stacks [9–11]. To improve the bonding between these two layers, a contact layer may be used. The contact layer material should ideally be chemically compatible with both the oxygen electrode and the coated interconnect, have a high electrical conductivity and high strength, as well as having a thermal expansion coefficient matching the other cell components.

Ceramic perovskite oxides such as (La,Sr)MnO₃ (LSM), (La,Sr)CoO₃ (LSC), (La,Sr)FeO₃ (LSF), and (La,Sr)(Co,Fe)O₃ (LSCF) are currently the most common choice for this application [12–14]. The perovskite oxides offer a high electrical conductivity and a thermal expansion coefficient matching the other cell components [12,15]. The main drawback with

using perovskite oxides as the contact layer is the high temperature (around $1100 \text{ }^\circ\text{C}$) required to sinter these materials well [16]. The contact layer is typically applied in the “green state” on the manufactured cell and sintered during stack assembly/sealing. Due to the use of steel interconnects and glass(-ceramic) seals, the typical stack assembly/sealing temperature is limited to approximately $900 \text{ }^\circ\text{C}$ [17]. This results in insufficient sintering of the contact layer and, as a consequence, a weaker bonding at the interface with an increased risk of contact loss during operation and thermal cycling.

Several suggestions to improve the perovskite oxide contact layer have been put forth. Sintering aids such as CuO have been added to enhance densification at a lower temperature [18] and glasses or inorganic binders have been mixed with the perovskite oxide to make a composite contact layer [13,19]. However, these solutions have been shown to have some drawbacks, such as limited long-term stability or poor compatibility with the oxygen electrode [18].

A promising method to achieve high density at a low sintering temperature is through the concept of “reactive oxidative bonding”, illustrated in Fig. 1. In this approach, the contact layer is applied in the form of metal particles that oxidize during stack assembly/sealing. Due to the high enthalpy of the oxidation reaction, the driving force for sintering is greatly enhanced compared to the driving force during conventional sintering of oxide particles. This approach was previously

* Corresponding author.

E-mail address: ilarit@dtu.dk (I. Ritucci).

<https://doi.org/10.1016/j.jeurceramsoc.2020.11.021>

Received 11 August 2020; Received in revised form 10 November 2020; Accepted 11 November 2020

Available online 13 November 2020

0955-2219/© 2020 The Authors. Published by Elsevier Ltd. This is an open access article under the CC BY license (<http://creativecommons.org/licenses/by/4.0/>).

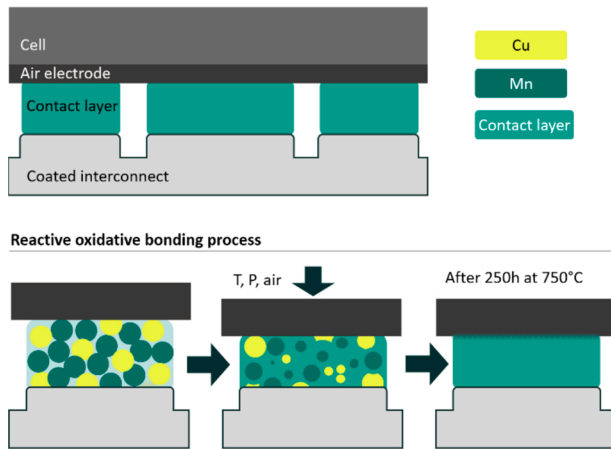


Fig. 1. Illustration of the cell-interconnect interface and the reactive oxidative bonding process. Cu and Mn are used here as an example. CL = contact layer.

used for fabricating contact layers based on Ni-Co [20], Co-Mn [21] and Ni-Fe [22].

In this study, we investigate the possibility of using mixtures of metallic Cu-Mn or Co-Mn particles deposited by screen printing to form the contact layer. The metallic particles are mixed in stoichiometric amounts to in-situ form the spinels $\text{Cu}_{1.2}\text{Mn}_{1.8}\text{O}_4$ [23] and MnCo_2O_4 [23,24] during a relatively mild heat treatment / sintering similar to that used in the assembly procedure of an SOC stack. The contact layers are characterized by measuring the area specific resistance and fracture toughness. The microstructural and compositional development of the contact layers is characterized by X-ray diffraction and electron microscopy.

2. Experimental

2.1. Contact layer preparation

Contact layer pastes for screen printing were prepared by mixing metallic powders with a solvent and organic binders to achieve a solid load of 70–72 wt.%. The CuMn contact layer was made with a mixture of 43 wt.% Cu (2 μm , Alfa Aesar) and 57 wt.% Mn (2 μm , American Elements), while the CoMn contact layer was made with a mixture of 66 wt.% Co (1.6 μm , Alfa Aesar) and 34 wt.% Mn (2 μm , American Elements). The specific Cu/Mn and Co/Mn ratios were chosen in order to form the spinel phases $\text{Cu}_{1.2}\text{Mn}_{1.8}\text{O}_4$ and MnCo_2O_4 after oxidation.

2.2. Chemical and microstructural characterization

For chemical and microstructural characterization, the contact layers were screen printed on top of $2 \times 2 \text{ cm}^2$ coupons of untreated Crofer 22 APU (VDM metals, Germany, [25]). The coupons were subsequently sintered in air following a representative SOC stack assembly/sealing procedure developed for a glass-ceramic sealant [26]. This procedure involved heating to 200 °C at 15 °C/h, holding for 2 h and heating to 400 °C at 15 °C/h, holding for 2 h (debinding), heating at 600 °C at 100 °C/h, holding for 1 h, heating to 700 °C at 100 °C/h, heating to 800 °C at 50 °C/h, holding for 1 h and finally cooling down to room temperature at 120 °C/h. After this sintering procedure, some of the samples were subsequently aged in air at 750 °C for 250 h.

Chemical and microstructural analyses were performed by Scanning Electron Microscopy (SEM) and energy-dispersive X-ray spectroscopy (EDS) (Hitachi TM3000 and ZEISS Merlin) either on the sample surface or on the sample embedded in epoxy resin (EpoFix, Struers) to investigate the cross-section. X-ray diffraction (XRD) analyses were performed on the samples surface using an XRD Bruker D8 diffractometer with Cu $K\alpha$ radiation. The spectra were collected from 15° to 75° 2 θ with a step

size of 0.02°, a collection time of 1 s per step and a 6 mm divergence slit.

2.3. Area specific resistance measurements

The electrical performance of the contact layers was evaluated by measuring the area specific resistance (ASR) in air at 750 °C. The set-up for the ASR measurement was explained in detail in ref. [27]. The contact layers were screen printed onto $20 \times 40 \text{ mm}^2$ plates of untreated AISI441 steel (0.3 mm thick) in a central area of $20 \times 20 \text{ mm}^2$. The samples were dried at 90 °C for 1 h to allow for handling. Pt wires were spot welded along the shorter edge of the steel plates to serve as voltage probes. Bisque-sintered $20 \times 20 \text{ mm}^2$ $\text{La}_{1-x}\text{Sr}_x\text{MnO}_3$ (LSM) pellets spray coated with a mixture of LSM (90 wt.%) and Co_3O_4 (10 wt.%) were used as current collecting plates to mimic the contact the contact layer would have with an SOC air electrode. The screen-printed steel samples and LSM pellets were stacked on top of each other as illustrated in Fig. 5.

Gold foils were connected to gold wires and placed on top and bottom of the stack for a chemically inactive current supply. A load of 7 kg was applied on top of the stack, corresponding to 17.5 N/cm². The stack was heated up to 800 °C following the sintering profile described in Section 2.2. A 2 A current was applied, corresponding to 0.5 A/cm², considering the nominal contact area of $20 \times 20 \text{ mm}^2$ between the steel plates and the LSM pellets. The stack was subsequently cooled down to 750 °C at 120 °C/h and the temperature was kept constant for 2000 h. The ASR was calculated from the voltage drop measured between the Pt wires placed between the different components: 1) contact layer/LSM, 2) LSM/LSM and 3) AISI441/LSM (see Fig. 5).

2.4. Fracture energy characterization

The adhesion of the contact layer to the steel interconnect was evaluated by measuring the critical energy release rate (G_c), here also referred to as fracture energy, of the interface between the contact layer and Crofer 22 H (VDM metals, Germany [28]). A detailed description of the measurement method and set-up can be found in the literature [29–32]. Here, the contact layer pastes were screen printed onto two $29 \times 3 \text{ mm}^2$ Crofer 22 H bars (0.5 mm thick) and dried at 90 °C for 1 h to allow for handling. The screenprinting resulted in a 70 μm thick contact layer. The two bars were placed on top of a $60 \times 3 \text{ mm}^2$ Crofer 22 H bar (0.5 mm thick), and bonded by heat treatment as described in Section 2.2. A load of 16.7 N/cm² was applied during the heat treatment.

Testing of the samples took place in air at room temperature using a four-point bending rig built at DTU Energy [30,33]. This test enables the measurement of the critical energy release rate for crack propagation at the interface of two layers [32,34,35]. It has previously been used to test the adherence between steel and a glass-ceramic sealant [36,37].

The sample was placed between two inner pins, 25 mm distant, and two outer pins, 50 mm distant. Bending was induced by a movement of the inner pins with a fixed displacement rate of 0.01 mm/s. During the measurement, both load and displacement were recorded. The fracture energy G_c was evaluated following the method derived by Charalambides et al. and later modified by Hofinger [32,34]. The maximum load, P , which is achieved at the crack propagation, was used to calculate the bending moment, M_b , between the inner pins in the four-point bending rig:

$$M_b = \frac{Pl}{2b} \quad (1)$$

where b is the sample width, 3.0 mm, and l is the distance between the outer and inner pins, 12.5 mm.

G_c , was estimated, using the analysis made by Charalambides and later modified by Hofinger:

$$G_c = \frac{M_b^2 (1 - \nu_2^2)}{2 E_2} \left(\frac{1}{I_2} - \frac{1}{I_c} \right) \quad (2)$$

where E_2 , ν_2 and I_2 , are the Young's modulus, Poisson's ratio and second moment of area of the through-going substrate of Crofer 22 H, respectively. I_c is the combined second moment of area of the stiffeners (metal bars) and the contact layer. The indexes 2 and d here refer to the contact layer and the substrate (long metal bar), respectively.

The second moments of areas are calculated as:

$$I_2 = \frac{h_2^3}{12} \quad (3)$$

where h_2 is the thickness of the substrate.

I_c is given by:

$$I_c = \frac{h_2^3}{3} + \kappa \frac{h_1^3}{3} + \mu \left(\frac{h_d^3}{3} + h_d^3 h_1 + h_1^2 h_d \right) - \frac{[h_2^2 - \kappa h_1^2 - \mu (h_d^2 + 2 h_1 h_d)]^2}{4 (h_2 + \kappa h_1 + \mu h_d)} \quad (4)$$

where the index 1 refers to the stiffener (the short metal bars). κ is the ratio between the stiffness of the substrate and the stiffener:

$$\kappa = \frac{E_1 (1 - \nu_2^2)}{E_2 (1 - \nu_1^2)} \quad (5)$$

And μ is the ratio between the stiffness of the substrate and the contact layer:

$$\mu = \frac{E_d (1 - \nu_2^2)}{E_2 (1 - \nu_d^2)} \quad (6)$$

where ν are the Poisson's ratios and E the Young's moduli. All Poisson's ratio was assumed to be 0.3, as no precise measurement was available and they do not influence the final estimated fracture energy (<0.1%). The Young's moduli was taken from the literature: $E_1 = 124$ GPa [38], $E_2 = E_d = 208$ GPa [28]. In this specific case, stiffener and substrate were identical (Crofer 22 H).

To ensure reproducibility and account for variations in sample preparation, four samples of each type were prepared and tested.

3. Results

3.1. X-ray diffraction

XRD patterns of the CuMn contact layer after sintering (at 800 °C) and after ageing for 250 h at 750 °C in air are shown in Fig. 2a and b respectively. After sintering, three crystalline phases can be detected: $\text{Cu}_{1.2}\text{Mn}_{1.8}\text{O}_4$ (Fig. 2c, cubic, Fd-3 m), CuO (Fig. 2d, monoclinic, C2c) and Mn_2O_3 (Fig. 2e, cubic, Ia3). No additional phases were detected after ageing, but the intensity of the peaks assigned to $\text{Cu}_{1.2}\text{Mn}_{1.8}\text{O}_4$ increased.

XRD patterns of the CoMn contact layer after sintering (at 800 °C) and after ageing at 750 °C for 250 h are shown in Fig. 2f and g. Three crystalline phases were identified after sintering: Co_3O_4 (Fig. 2j, cubic, Fd-3 m), Mn_2O_3 (Fig. 2i, cubic, Ia3), and Co_2MnO_4 (Fig. 2h, cubic, Fd3 m). After ageing, no new phases were found, but the intensity of the MnCo_2O_4 peaks increased.

3.2. Microscopy

SEM micrographs and EDS maps of the CuMn contact layer on Crofer 22 APU after sintering at 800 °C are shown in Fig. 3a and b. At least two different phases can be distinguished on the top surface (Fig. 3a), both from the contrast difference in the backscattered electron (BSE) image and from the EDS maps of Mn and Cu. According to quantitative EDS point analysis of the two areas, the lighter grey area is composed of mainly Cu (81.4 wt.%) and O (18.7 wt.%), while the darker grey area is composed of Cu (35.9 wt.%), Mn (36.8 wt.%) and O (27.2 wt.%). The

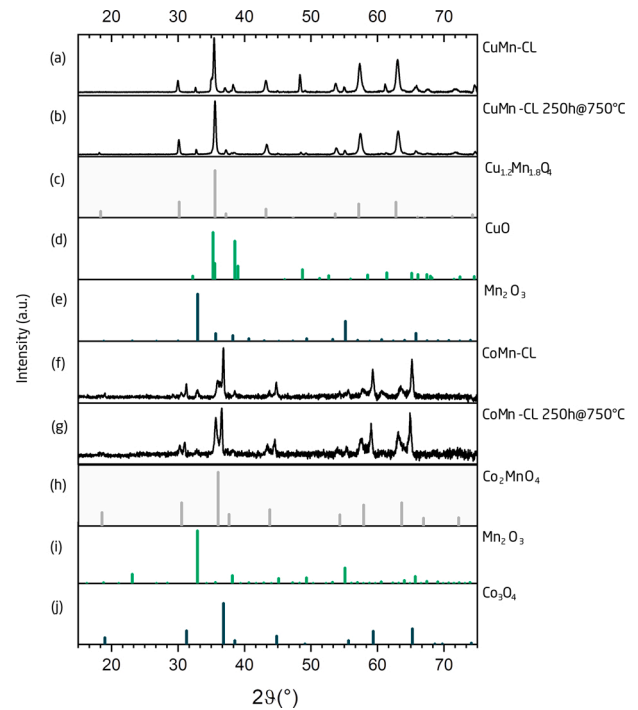


Fig. 2. XRD patterns for the two contact layer compositions studied, CuMn-CL and CoMn-CL, after sintering at 800 °C (black) and after ageing at 750 °C for 250 h. $\text{Cu}_{1.2}\text{Mn}_{1.8}\text{O}_4$ =PDF 01-071-1144, CuO = PDF 01-089-2530, Mn_2O_3 =PDF 01-076-0150, Co_2MnO_4 = PDF00-023-1237, Co_3O_4 =PDF 00-043-1003.

latter corresponds to the composition $\text{Cu}_{1.3}\text{Mn}_{1.6}\text{O}_{4.1}$. Considering the XRD results (Section 3.1) the light grey phase likely corresponds to CuO, while the dark grey phase corresponds to the spinel phase. The Mn_2O_3 phase could not be detected on the surface based on the EDS results.

From the cross-section micrograph of the same sample (Fig. 3b), it can be seen that the CuO phase (light grey) is mainly present on the surface of the sample, in addition to the spinel phase. Based on the difference in contrast in the BSE image, the bulk of the contact layer consists also of two phases. According to quantitative EDS point analysis, the composition of the lighter grey phase is Mn 43.3 wt %, Cu 32.2 wt % and O 24.5 wt %, while the composition of the darker grey phase is Mn 69.8 wt %, O 28.6 wt % and Cu 1.5 wt %. Based on this and the XRD results, the former is likely the spinel phase, while the latter is the Mn_2O_3 .

Fig. 3c and d show a SEM micrograph and EDS maps of the CuMn contact layer surface after ageing for 250 h at 750 °C. The surface (Fig. 3c) is now homogenous and composed of Cu (45 wt.%), Mn (34 wt.%) and O (21 wt.%). No other phases can be detected. Inspection of the cross section (Fig. 3d) confirms that the light grey layer of CuO has disappeared from the surface. The majority of the contact layer consists of a homogenous mixture of Cu (between 31–28 wt.%), Mn (between 44–48 wt.%) and O (25–24 wt.%). A single CuO particle (Cu 83 wt % and O 17 wt %) was detected in the middle of the contact layer. This is likely due to insufficient mixing of the green powders in the screen-printing paste.

SEM micrographs and EDS maps of the CoMn contact layer on Crofer 22 APU after sintering at 800 °C are shown in Fig. 4a and b. The surface analysis (Fig. 4a) indicates the presence of two phases. According to quantitative EDS point analysis, one phase is composed mainly of Co (75 wt.%), O (19 wt %) and a small fraction of Mn (6 wt %), while the other phase is composed of Co (39 wt %), Mn (39 wt %) and O (22 wt %). Taking into account the XRD results presented in Section 3.1, the two phases are likely Co_3O_4 and $(\text{Mn},\text{Co})_3\text{O}_4$ spinel, respectively.

The cross section of the same sample (Fig. 4b) shows that the CoMn

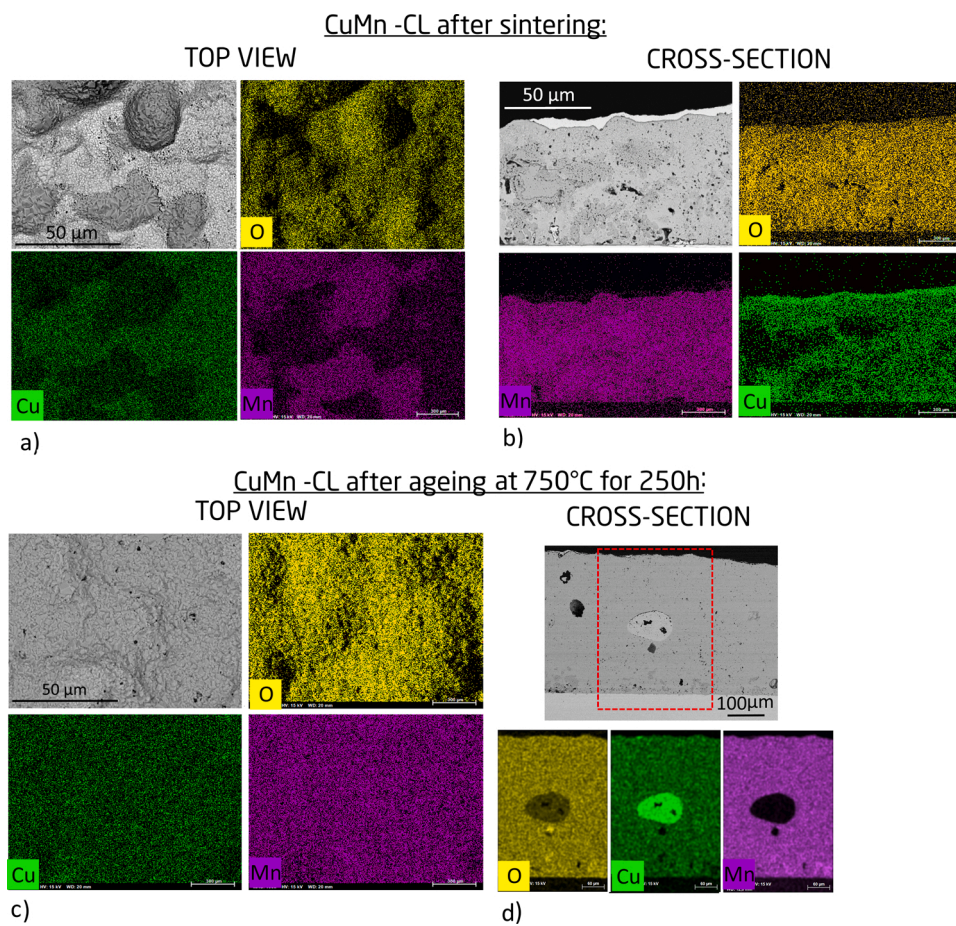


Fig. 3. SEM/EDS micrographs of CuMn CL after sintering, top view (a) and cross-section (b) and after ageing at 750 °C for 250 h, top view (c) and cross-section (d). The EDS maps in (d) correspond to a small area of the micrograph which is limited by the red dotted frames. (For interpretation of the references to colour in this figure legend, the reader is referred to the web version of this article.)

contact layer after sintering at 800 °C consists of large, dense agglomerates with finer particles between. According to EDS analysis the larger agglomerates consist of a Mn-oxide core covered by a shell composed of 32 wt% Co, 37 wt% Mn and 32 wt% O. The finer particles are composed of 73 wt% Co and 27 wt% O. The CoMn contact layer is clearly more porous than the CuMn contact layer (cf. Fig. 4).

SEM micrographs and EDS maps of the CoMn contact layer after ageing for 250 h at 750 °C are shown in Fig. 4c and d. The top view micrograph (Fig. 4c) shows that the contact layer surface has not densified further with ageing compared to after sintering. The surface also remains inhomogeneous after ageing, as some areas with only Co (73 wt%) and O (27 wt%) can be detected in the area with the finer particles. The cross section of the same sample (Fig. 4d), shows that the Mn found in the core of the agglomerate after sintering at 800 °C now, after ageing at 750 °C, has fully inter-diffused with Co and O. The composition according to EDS point analysis (39 wt% Co, 38 wt% Mn and 23 wt% O) indicates that the larger particles are the CoMn spinel. Also, after ageing at 750 °C, the CoMn contact layer is significantly more porous than the CuMn contact layer after ageing.

3.3. Area specific resistance

The ASR measured during ageing at 750 °C is plotted in Fig. 5. The ASR of 441 steel increases throughout the whole measurement and reaches 54.4 mΩ cm² after 2000 h of ageing due to oxidation. The ASR increase of the 441 steel is largest during the first 300 h of ageing, after this, the ASR increases almost linearly with time. With the addition of a CoMn or CuMn contact layer to the 441 steel, the ASR decreases slightly

during the first 500 h, before it reaches a plateau and remains nearly constant for the next 1500 h. After 2000 h of ageing at 750 °C, the ASR is 23 mΩ cm² for the sample with a CoMn contact layer and 21 mΩ cm² for the sample with a CuMn contact layer, i.e. less than half of the ASR measured for the 441 steel.

During the first 500 h, the ASR measured over a single LSM plate shows a similar trend as the ASR of the samples with contact layers. With further ageing, the ASR of LSM continues to decrease, but at a slower rate. The stack of samples experienced one unplanned thermal cycle around 450 h. This did not influence the results significantly as the ASR values followed the same trend before and after the thermal cycle.

3.4. Fracture energy

Fig. 6f shows a representative plot of the load-displacement curve recorded during the four-point bending test. While bending the samples at a continuous rate, the load first increased to the point of the first crack growth and then continued in a saw tooth pattern. The jagged load response is the result of fast crack growth and arrestment. The fracture energy is evaluated using the load peaks, which corresponds to the load where the crack stopped propagating, as discussed further in Section 4.

The fracture energy, G_c for each contact layer after sintering at 800 °C and after ageing at 750 °C for 250 h is reported in Table 1. Note that the G_c after ageing decreased to 37 % and 65 % of the G_c value after sintering for the CuMn and the CoMn contact layers, respectively.

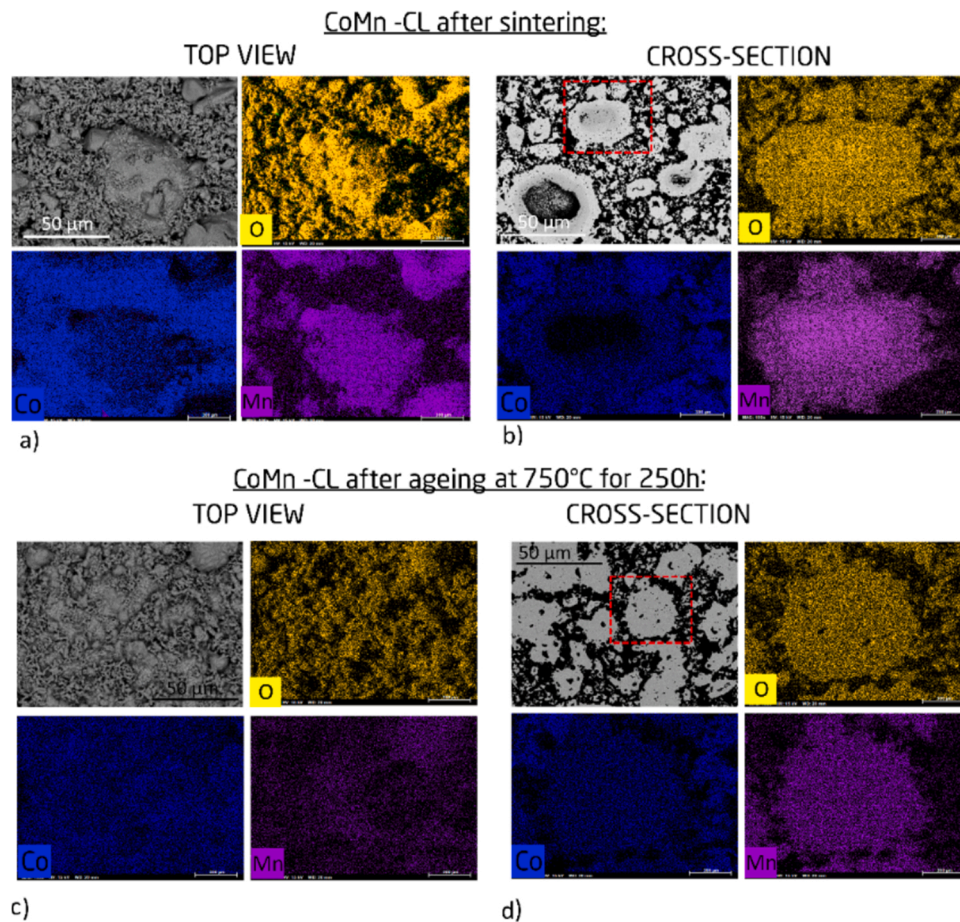


Fig. 4. Overview SEM micrographs and EDS maps of CoMn after sintering, top view (a) and cross-section (b) and after ageing 250 h at 750 °C, top view (c) and cross-section (d). The EDS maps in (b) and (d) correspond to a small area of the micrograph which is limited by the red dotted frames. (For interpretation of the references to colour in this figure legend, the reader is referred to the web version of this article.)

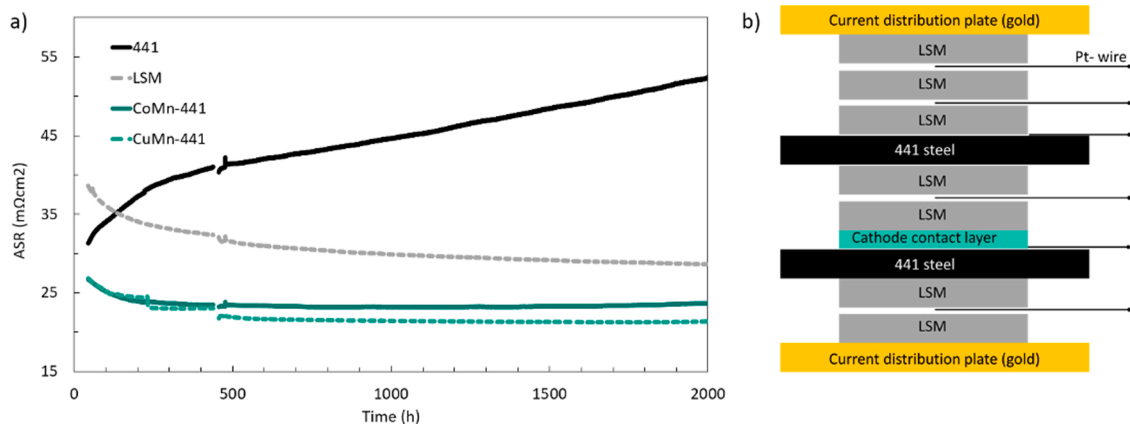


Fig. 5. a) ASR values of 441, LSM and the contact layers measured at 750 °C in air, b) illustration of the set-up used for the ASR measurements.

3.5. Fractography and microstructural analysis

After the fracture toughness test, the unbroken part of the sample sandwiches was manually broken apart to analyse the fracture surfaces by SEM/EDS. As illustrated by the sketches in Figs. 6a and 7 a the analysis was made on the area closest to the notch of the sample, corresponding to the area fractured during the four-point bend test.

The different layers (i.e. steel, oxide scale, contact layer) of each sample contain elements that are unique to that layer. By comparing the

EDS maps on each side of the fractured sample, the layer or interface where the crack propagation occurred can be identified. Specifically, the combination of Cu (green) and Mn (purple) in the same layer identify the CuMn contact layer, the combination of or Mn (purple) and Co (blue) in the same layer identify the CoMn contact layer, Fe (orange) identifies the Crofer 22 H substrate, while Cr (red), without Fe, identifies the oxide scale of Crofer 22 H.

Fig. 6b to e shows the fracture surface of the CuMn contact layer after sintering at 800 °C. According to the EDS maps (Fig. 6b) the majority of

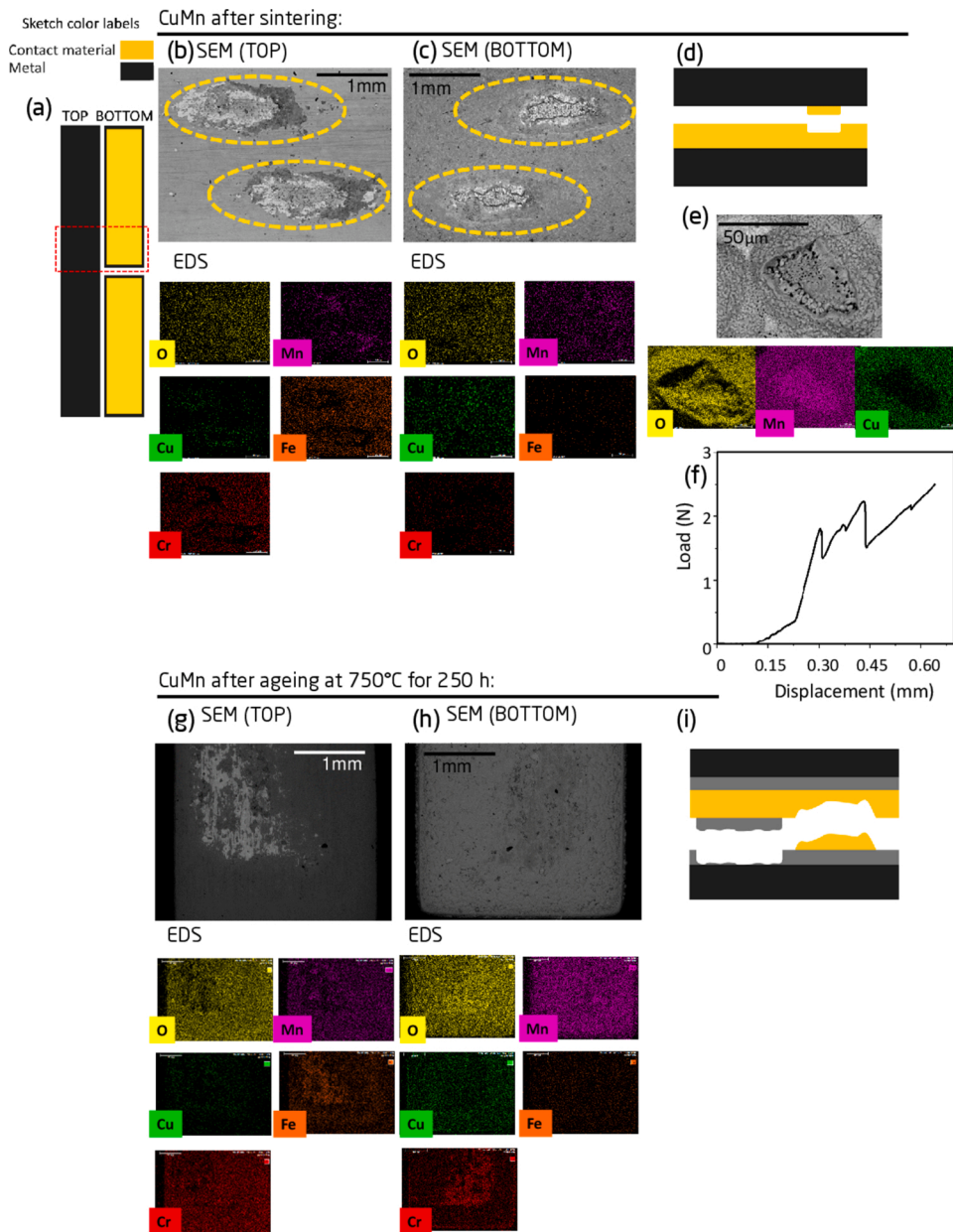


Fig. 6. SEM micrographs and EDS maps of CuMn contact layer after sintering at 800 °C (a) sketch of sample with the analysed area indicated by a stippled rectangle. (b) fracture surface, top bar and (c) bottom bar. (d) Schematic of the fracture mechanism (e) higher magnification SEM and EDS. (f) An example of recorded load-displacement curves. SEM micrographs and EDS maps of CuMn contact layer after ageing at 750 °C for 250 h, top bar (g) and bottom bar (h). Schematic of the fracture mechanism (i).

Table 1

Measured fracture energies for the two contact layers after sintering at 800 °C and after ageing at 750 °C for 250 h. CL = contact layer.

	CuMn CL	After ageing	CoMn CL	After ageing
G_C (J/m^2)	13.5	5.0	6.0	3.9
Std. dev. (J/m^2)	3.2	1.6	1.6	0.9

the surface of the top bar is composed of Fe, Cr and Mn. These elements can be assigned to the Crofer 22 H substrate and the oxide scale thermally grown on the substrate during the sintering heat treatment (i.e. Cr_2O_3 and $(Mn,Cr)_3O_4$). The areas in Fig. 6b highlighted by yellow dashed ellipses are rich in Cu and Mn and can accordingly be assigned to the CuMn contact layer. On the equivalent area of the bottom bar (Fig. 6c), Cu, Mn, and Cr are detected. The Mn and Cr can be assigned to the oxide scale formed on the Crofer 22 H during the sintering, while the Cu identifies areas covered by the CuMn contact layer.

A higher magnification image of the fracture surface is shown in

Fig. 6e. According to the EDS maps, in the fractured area there is a nucleus of oxidized Mn, covered by a shell of Mn, Cu and O.

The above analysis of the fracture surface indicates that the crack mainly propagates at the interface between the contact layer and the oxidized Crofer 22 H substrate, and to only a limited extent within the contact layer itself. The fracture pattern is schematized in Fig. 6d.

Fig. 6g to i shows the fracture surface of the CuMn contact layer after ageing at 750 °C for 250 h. EDS analysis of the surface of the top bar (Fig. 6g) shows that most of this surface is covered by Fe, Cr and Mn. All of these elements can be assigned to the Crofer 22 H substrate and thermally grown oxide scale. In addition, a small area of the surface has a relatively higher concentration of Fe. This area corresponds to the brightest contrast areas in the SEM-BSE image and may be assigned to the steel substrate (i.e. no oxide scale). The corresponding area of the bottom bar has two main compositions present: one rich in Cu and Mn, and one rich in Cr. The Cr-rich area of the bottom bar corresponds to the Fe-rich area found on the top bar. Based on these results, as schematized in Fig. 6i, it is possible to conclude that the crack propagates primarily through the $(Mn, Cr)_3O_4$ oxide scale on the Crofer 22 H substrate, and

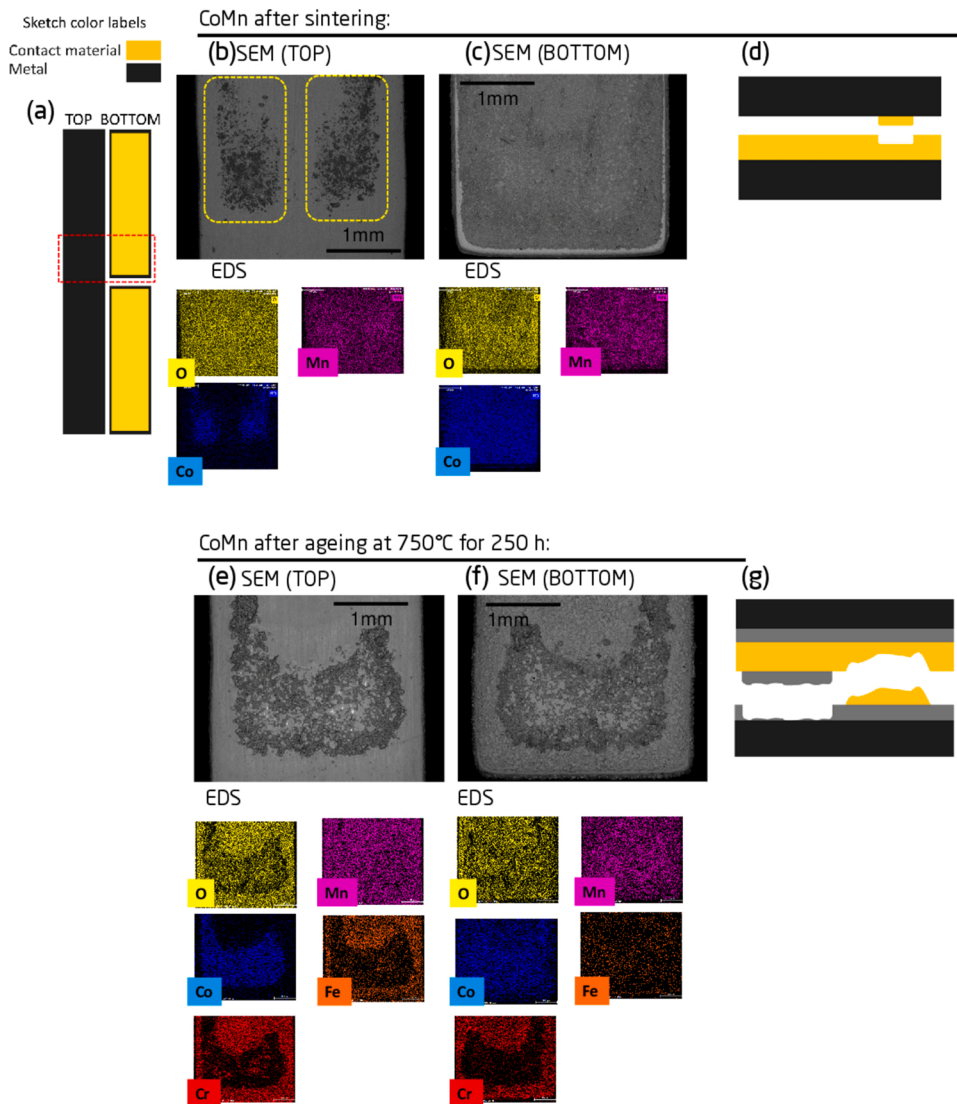


Fig. 7. Overview of SEM micrographs and EDS maps of CoMn contact layer after sintering at 800 °C. A sample with highlighted analysed area (a). CoMn on Crofer 22 H (b) top bar SEM and EDS and (c) bottom bar SEM and EDS. The sketch of the fracture mechanism in (d). Overview of SEM micrographs and EDS maps of CoMn contact layer after ageing at 750 °C for 250 h: CuMn on Crofer 22 H (e) top bar SEM and EDS and (f) bottom bar SEM and EDS. The sketch of the fracture mechanism in (g).

partly through the contact layer.

Fig. 7b–d show the fracture surface of the CoMn contact layer after sintering at 800 °C. EDS maps from the surface of the top bar (Fig. 7b) show that mainly Mn is present in the lighter contrast areas of the SEM-BSE image in addition to Fe and Cr (EDS maps for these are not shown). These elements can be assigned to the Crofer 22 H substrate. The darker contrast areas (highlighted by yellow dashed ellipses in Fig. 7b) are rich in Co and Mn and can accordingly be assigned to the CoMn-contact layer. EDS maps of the surface of the bottom bar (Fig. 6f), show the presence of Co, Mn, and O, which can be assigned to the CoMn contact layer. Based on these results, it may be concluded that the crack propagates mainly at the interface between the CoMn contact layer and the Crofer 22 H substrate, and only to a lower extent within the contact layer. This is schematically illustrated in Fig. 7d.

Fig. 7e–g show the fracture surface of the CoMn contact layer after ageing at 750 °C for 250 h. On the central part of the surface of the top bar (Fig. 7e) mainly Co and Mn are detected, identifying the CoMn contact layer. The surrounding area is rich in Fe, Cr and Mn, indicating the presence of the Crofer 22 H substrate and a $\text{Cr}_2\text{O}_3/(\text{Mn,Cr})_3\text{O}_4$ oxide scale. On the bottom bar (Fig. 7f), the central part of the surface contains Co, Mn and O, while the surrounding area is Cr-rich. I.e. the central area corresponds to the contact layer while the surrounding area corresponds to the $\text{Cr}_2\text{O}_3/(\text{Mn,Cr})_3\text{O}_4$ oxide scale. These observations indicate that the crack propagates within the CoMn contact layer in the central part of

the fractured area, while in the outer part it propagates at the interface between the oxide scale and the Crofer 22 H, as schematically illustrated in Fig. 7g.

4. Discussion

4.1. Mechanical properties

For both the CoMn and the CuMn contact layers, high energy release rates of 6.0 J/m² and 13.5 J/m², respectively, were measured on the as-prepared samples. Also after 250 h of ageing at 800 °C the fracture energies measured (3.9 J/m² for CoMn and 5.0 J/m² for CuMn) are 4–5 times higher compared to state-of-the-art contact materials like LSM and LSC [14], as illustrated in Fig. 8.

The reason for the decrease in fracture energy during the 250 h of ageing can be related to the changes in the microstructure with time, and the associated changes in the crack paths, described in the following. As seen from the SEM image analysis, the as prepared CuMn contact layer sample consisted of larger Mn_2O_3 particles surrounded by more or less homogeneously distributed $\text{Cu}_{1.2}\text{Mn}_{1.8}\text{O}_4$ spinel (Fig. 3a–b). This structure resembles a composite material consisting of Mn_2O_3 filler material within a $\text{Cu}_{1.2}\text{Mn}_{1.8}\text{O}_4$ matrix.

After 250 h of ageing, the microstructure is more homogenous and Cu, Mn and O appear evenly distributed in the elemental maps

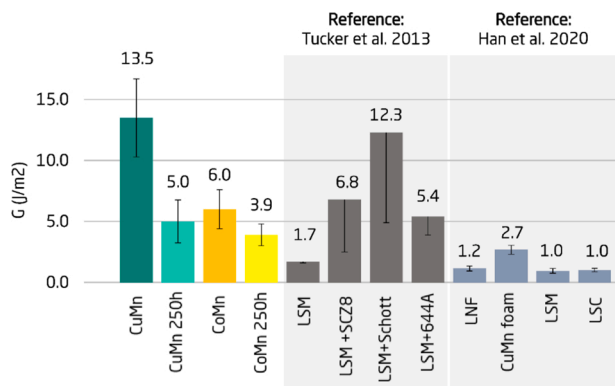


Fig. 8. Fracture energies for the two cathode contact layers: CuMn contact layer and CoMn contact layer, after sintering and after 250 h at 750 °C, and as a reference, the results from Tucker 2013 et al and Han et al 2020.

(Fig. 3c–d).

The possible crack paths in these two microstructures are expected to be different. In the as prepared sample, the crack path through the spinel phase/Mn₂O₃ particles composite is more tortuous as compared to the rather straight crack path expected in the aged sample with a more homogenous microstructure. The longer path induced by the tortuosity in the as prepared samples would result in a higher effective surface area and thus a comparatively higher surface energy.

Furthermore, the crack partially propagated through the oxide scale for both the aged CoMn and CuMn contact layer. The oxide scale, which is also a brittle ceramic layer, grows during the ageing and is apparently a weaker layer compared to the contact layer, as the crack prefers to grow in this layer. Residual stresses from the oxide scale growth could also play a role, but the scale is situated on a much stiffer substrate, and insignificant energy is released by the crack growth. The weakening of the contact layer/interconnect interface could thus possibly be avoided by a better protection of the steel. The oxide scale layer was not taken into account in the calculation for the fracture energy. This layer is few microns thick, and it does not influence significantly the calculations.

These hypotheses could explain the decrease in G_c and the lower load measured to initiate and propagate the crack after ageing.

A comparable microstructural development was found for the CoMn contact layer. As seen in the SEM images of the as prepared sample (Fig. 4), MnCo₂O₄ spinel is formed on the surface of the Mn₂O₃ particles, resulting in essentially a composite layer. After 250 h of ageing, the microstructure is significantly homogenized, which again may be the explanation for the lower fracture energy measured in the aged samples (in addition to the formation of the oxide scale).

Compared to the CuMn contact layer, the CoMn contact layer has a significant higher porosity. This is consistent with the higher sintering temperatures typically needed for the formation of a dense CoMn spinel (1100 °C) [39]. The higher porosity is most likely the reason for the lower fracture energy measured for the CoMn contact layer compared to the CuMn contact layer.

In addition to a higher fracture toughness, the inhomogeneous microstructure also gives rise to a more uneven crack propagation, which can be seen on the recorded load-displacement curve in Fig. 6f. For a homogeneous material, the load would reach a plateau when the displacement is at a continuous rate due to a continuous crack propagation. The load plateau is usually used to determine the G_c (using Eq. (2)). In this case, the load did not reach a plateau because of the inhomogeneous microstructure. Instead, the "plateau" consists of several, clearly distinguishable peaks. A possible explanation for this is that the crack comes to a halt at irregularities within the sample, where the fracture energy is built up until it becomes high enough for the crack to propagate further through these higher toughness areas. Simultaneously, the crack propagates swiftly through the more homogeneous

material behind (resulting in the sudden drop in load after each peak). During real operation, the high toughness areas would stop a propagating crack. For this reason, the peaks are used to calculate the critical fracture energy, G_c , for the contact layer.

4.1.1. Comparison with state-of-the-art described in literature

As seen in Fig. 8, other attempts to increase the interface adherence of contact layers have been researched in past studies. The highest fracture energy is 12.3 J/m², reported by Tucker et al., which was achieved by mixing glass into the contact layer material to join Mn_{1.5}Co_{1.5}O₄ coated AISI441 steel at 1000 °C. Although the addition of glass improved the mechanical properties, the insulating properties of the glass negatively influenced the electrical performance of the contact layer [35]. A compromise with a lower amount of glass added showed a sufficiently high conductivity, but the fracture energy was only 5.4 J/m². It should be pointed out that a high assembly temperature of 1000 °C was used in the preparation of these samples, i.e. 200 °C more than in this study. As mentioned before, such high temperatures could be damaging to some components of the SOC stack.

Another study from Han et al. (see Fig. 8 [14]) investigated the suitability of several materials as contact layers between a LSC/CGO oxygen electrode and a Co or MnCo₂O₄ coated metallic interconnect. The highest fracture energy (8.6 J/m²) reported in this study was achieved with the use of metallic CuMn foam as contact layer. It should be noticed that all values reported in this study were for as prepared samples, and the influence of ageing on the interface stability was not investigated. Han et al. reported that the interconnect coating can significantly influence the robustness of the interface. This indicates that the interface stability in the here reported system, i.e. bare steel without coatings, could possibly be further increased. Also in terms of up-scalability the here presented route (simple use of metallic Cu and Mn or Co powder) is more promising because; i) the production cost of the CuMn foam is expected to be more expensive due to the complex processing route, ii) and the foam needs to be applied over the complete cell area while the CuMn powders can be selectively printed at the contact points between the interconnect and the oxygen electrode.

4.2. Electrical properties

The ASR measured for the 441 steel contacted to LSM increased rapidly during ageing at 750 °C and reached 54.4 mΩ cm⁻² after 2000 h. This behaviour is similar to the ASR values previously reported in literature when using a comparable measurement set-up. For example, Stevenson et al. [40] reported that the ASR of 441 after 2000 h at 800 °C was ~ 35 mΩ cm⁻² while Molin et al. [27] reported that the ASR of bare Crofer 22 APU was around 45 mΩ cm⁻² after 40,000 h of ageing at 750 °C. The high resistance and increase in ASR with time can be attributed to the growth of poorly conductive oxide scales on the steel surface. In case of the 441 steel, formation of Cr₂O₃ and SiO₂ likely dominate the measured ASR [40]

By applying a CuMn or CoMn contact layer between the 441 steel and LSM contacting plate, the ASR is decreased to less than half and remains nearly constant with time. As discussed above, the CuMn and CoMn contact layers are oxidized during heat-up of the stack to form well-conductive Cu_{1.3}Mn_{1.7}O₄ (225 S/cm at 750 °C [23]) and MnCo₂O₄ (89 S/cm at 800 °C [24]), respectively. Since the electrical conductivity of these oxides is much larger than the conductivity of the native oxide scale formed on the steel (~0.01–0.1 S/cm for Cr₂O₃ at 800 °C [41,42]) it may be concluded that the contact layers do not contribute significantly to the resistance of the interconnect. Instead, the results here show that the contact layers improve the ASR of the 441 steel contact layer assembly.

The improvement in ASR achieved with the application of the contact layers is similar to the improvements previously observed by application of protective coatings such as Mn_{1.5}Co_{1.5}O₄, MnCo₂O₄ and MnCo_{1.7}Cu_{1.3}O₄ [24,40,43]. This is not surprising considering that the

composition and structure of the oxidized contact layers is very similar to that of the protective coatings, i.e. Mn and Co/Cu-based spinel oxides. An important distinction is that the coatings tested in previous works were prepared by depositing an oxide powder (by spraying or electrophoretic deposition) and subsequently heat treating the coating in two-steps in order to densify it [24,40,43]. Here, a comparable protection is achieved by in-situ sintering of the contact layer. An even greater reduction in ASR may be achieved by combining the contact layers with a CeCo coating on the 441 steel, as shown in [44].

The CuMn contact layer resulted in a slightly lower ASR than the CoMn contact layer, but the differences are almost within the uncertainty of this type of ASR measurement, where porous LSM is used as the contacting surface. As seen in Fig. 5, the ASR measured over the LSM contacting plate alone decreases with time. This can be attributed to creep and sintering of the contacting plate, resulting in a change in the effective contacting area with time [43,45,46]. Although this somewhat masks the changes in ASR of the other samples, the use of lightly sintered LSM plates provides a more realistic measurement of the contacting between the cell and the interconnect in a real SOC stack compared to using Pt or other noble metals [47,48].

5. Conclusions

In this work a novel route for processing a robust and well conducting contact layer between the solid oxide cell air electrode and the interconnect has been demonstrated. The concept utilizes the reactive energy of the in-situ oxidation of Cu + Mn or Co + Mn metallic powders at high temperature to ensure interdiffusion into neighbouring surfaces and assist the sintering to form a denser and better adhering contact layer.

Both the CuMn and the CoMn contact layer resulted in very high fracture energies after sintering of 13.5 J/m² and 6.0 J/m², respectively. This is considerably tougher than the conventional perovskite contact layers of 1–2 J/m², when sintered at the same low temperatures. The higher fracture energy of the CuMn contact layer was attributed to the formation of a denser layer. The fracture energy decreased to 5.0 J/m² for the CuMn contact layer and 3.9 J/m² for the CoMn contact layer after ageing at 750 °C for 250 h. Microscopy indicated that the failure after ageing primarily occurred within the oxide scale. Thus, the decrease in the fracture energy after ageing was primarily because the 441 steel substrate was uncoated and formed a weak oxide scale.

Relatively low area specific resistances (ASR) of 21–23 mΩ cm² were measured for the contact layer/interconnect steel assembly. The electric resistance of the thermally grown oxide scale on the steel was suggested as the main contribution to the ASR. The contact layers reduced the increase in ASR over time compared to bare steel, showing that the contact layers partially protected the steel against oxidation.

Declaration of Competing Interest

The authors declare that they have no known competing financial interests or personal relationships that could have appeared to influence the work reported in this paper.

Acknowledgements

This work is a part of the project LOWCOST-IC, which has received funding from the Fuel Cells and Hydrogen 2 Joint Undertaking (JU) under grant agreement No 826323. The JU receives support from the European Union's Horizon 2020 research and innovation programme and Denmark, France, Austria, Belgium, Sweden, Germany, Italy.

The authors would like to thank E. Abdellahi and J. Johnson for the technical assistance.

References

- [1] Y. Zhao, C. Xia, L. Jia, Z. Wang, H. Li, J. Yu, Y. Li, Recent progress on solid oxide fuel cell: lowering temperature and utilizing non-hydrogen fuels, *Int. J. Hydrogen Energy* 38 (2013) 16498–16517, <https://doi.org/10.1016/j.ijhydene.2013.07.077>.
- [2] P. Kalra, R. Garg, A. Kumar, Solid oxide fuel cell - a future source of power and heat generation, *Mater. Sci. Forum.* 757 (2013) 217–241, <https://doi.org/10.4028/www.scientific.net/MSF.757.217>.
- [3] R.M. Ormerod, *Fuels and Fuel Processing. High-Temperature Solid Oxide Fuel Cells Fundam., Des. Appl., Elsevier Ltd, 2003*, pp. 333–361, <https://doi.org/10.1016/B978-185617387-2/50029-5>.
- [4] A. Nechache, M. Cassir, A. Ringuedé, Solid oxide electrolysis cell analysis by means of electrochemical impedance spectroscopy: a review, *J. Power Sources* (2014), <https://doi.org/10.1016/j.jpowsour.2014.01.110>.
- [5] A. Hauch, S.D. Ebbesen, S.H. Jensen, M. Mogensen, Solid oxide electrolysis cells: microstructure and degradation of the Ni/Yttria-stabilized zirconia electrode, *J. Electrochem. Soc.* 155 (2008) B1184, <https://doi.org/10.1149/1.2967331>.
- [6] S.D. Ebbesen, M. Mogensen, Electrolysis of carbon dioxide in solid oxide electrolysis cells, *J. Power Sources* 193 (2009) 349–358, <https://doi.org/10.1016/j.jpowsour.2009.02.093>.
- [7] J.C. Ruiz-Morales, D. Marrero-López, J. Canales-Vázquez, J.T.S. Irvine, Symmetric and reversible solid oxide fuel cells, *RSC Adv.* 1 (2011) 1403–1414, <https://doi.org/10.1039/c1ra00284h>.
- [8] H. Tu, U. Stimming, Advances, aging mechanisms and lifetime in solid-oxide fuel cells, *J. Power Sources* (2004) 284–293, <https://doi.org/10.1016/j.jpowsour.2003.09.025>.
- [9] D.N. Boccacini, O. Sevecek, H.L. Frandsen, I. Dlouhy, S. Molin, B. Charlas, J. Hjelm, M. Cannio, P.V. Hendriksen, Determination of the bonding strength in solid oxide fuel cells' interfaces by Schwickerath crack initiation test, *J. Eur. Ceram. Soc.* 37 (2017) 3565–3578, <https://doi.org/10.1016/j.jeurceramsoc.2017.04.018>.
- [10] L. Blum, An analysis of contact problems in solid oxide fuel cell stacks arising from differences in thermal expansion coefficients, *Electrochim. Acta* 223 (2017) 100–108, <https://doi.org/10.1016/j.electacta.2016.12.016>.
- [11] T.T. Molla, K. Kwok, H.L. Frandsen, Modeling the mechanical integrity of generic solid oxide cell stack designs exposed to long-term operation, *Fuel Cells* 19 (2019) 96–109, <https://doi.org/10.1002/face.201800081>.
- [12] W.J. Quadackers, H. Greiner, M. Hänsel, A. Pattanaik, A.S. Khanna, W. Malléner, Compatibility of perovskite contact layers between cathode and metallic interconnector plates of SOFCs, *Solid State Ion.* 91 (1996) 55–67, [https://doi.org/10.1016/s0167-2738\(96\)00425-0](https://doi.org/10.1016/s0167-2738(96)00425-0).
- [13] M.C. Tucker, L. Cheng, L.C. Dejonghe, Glass-containing composite cathode contact materials for solid oxide fuel cells, *J. Power Sources* 196 (2011) 8435–8443, <https://doi.org/10.1016/j.jpowsour.2011.05.055>.
- [14] L. Han, B. Talic, K. Kwok, P.V. Hendriksen, H.L. Frandsen, Interface fracture energy of contact layers in a solid oxide cell stack, *ACS Appl. Energy Mater.* (2020), <https://doi.org/10.1021/acsaem.9b02026>.
- [15] E.N. Naumovich, K. Zakharchuk, S. Obrębowski, A. Yaremchenko, (La,Sr)(Fe,Co)O₃-based cathode contact materials for intermediate-temperature solid oxide fuel cells, *Int. J. Hydrogen Energy* 42 (2017) 29443–29453, <https://doi.org/10.1016/j.ijhydene.2017.09.122>.
- [16] N. Shaigan, W. Qu, D.G. Ivey, W. Chen, A review of recent progress in coatings, surface modifications and alloy developments for solid oxide fuel cell ferritic stainless steel interconnects, *J. Power Sources* 195 (2010) 1529–1542, <https://doi.org/10.1016/j.jpowsour.2009.09.069>.
- [17] N.H. Menzler, F. Tietz, S. Uhlenbruck, H.P. Buchkremer, D. Stöver, Materials and manufacturing technologies for solid oxide fuel cells, *J. Mater. Sci.* 45 (2010) 3109–3135, <https://doi.org/10.1007/s10853-010-4279-9>.
- [18] W.J. Shong, C.K. Liu, C.W. Lu, S.H. Wu, R.Y. Lee, Characteristics of La 0.6 Sr 0.4 Co 0.2 Fe 0.8 O 3 -Cu 2 O mixture as a contact material in SOFC stacks, *Int. J. Hydrogen Energy* 42 (2017) 1170–1180, <https://doi.org/10.1016/j.ijhydene.2016.08.211>.
- [19] M.C. Tucker, L. Cheng, L.C. Dejonghe, Inorganic binder-containing composite cathode contact materials for solid oxide fuel cells, *J. Power Sources* 224 (2013) 174–179, <https://doi.org/10.1016/j.jpowsour.2012.09.114>.
- [20] Z. Lu, G. Xia, J.D. Templeton, X. Li, Z. Nie, Z. Yang, J.W. Stevenson, Development of Ni1-xCoxO as the cathode/interconnect contact for solid oxide fuel cells, *Electrochem. Commun.* 13 (2011) 642–645, <https://doi.org/10.1016/j.elecom.2011.03.034>.
- [21] J.W. Stevenson, G.G. Xia, Z. Lu, X. Li, Z. Nie, T. Oh, J.D. Templeton, *Development of Cathode Contact Materials for SOFC Cathode/Interconnect Contact Materials*, 2010.
- [22] Y.T. Yu, J.H. Zhu, B.L. Bates, Effect of precursor materials on the performance of the NiFe 2 O 4 -based spinel layer for SOFC cathode-side contact application, *Solid State Ion.* (2018), <https://doi.org/10.1016/j.ssi.2018.05.030>.
- [23] A. Petric, H. Ling, Electrical conductivity and thermal expansion of spinels at elevated temperatures, *J. Am. Ceram. Soc.* 90 (2007) 1515–1520, <https://doi.org/10.1111/j.1551-2916.2007.01522.x>.
- [24] B. Talic, P.V. Hendriksen, K. Wiik, H.L. Lein, Thermal expansion and electrical conductivity of Fe and Cu doped MnCo₂O₄ spinel, *Solid State Ion.* 326 (2018) 90–99, <https://doi.org/10.1016/j.ssi.2018.09.018>.
- [25] VDM-Metals, VDM ® Crofer 22 APU, (2010) 10. http://www.vdm-metals.com/fileadmin/user_upload/Downloads/Data_Sheets/Datenblatt_VDM_Crofer_22_APU.pdf.
- [26] I. Ritucci, K. Agersted, P. Zielke, A.C. Wulff, P. Khajavi, F. Smeacetto, A.G. Sabato, R. Kiebach, A Ba-free sealing glass with a high coefficient of thermal expansion and

- excellent interface stability optimized for SOFC/SOEC stack applications, *Int. J. Appl. Ceram. Technol.* (2018) 1–12, <https://doi.org/10.1111/ijac.12853>.
- [27] S. Molin, P. Jasinski, L. Mikkelsen, W. Zhang, M. Chen, P.V. Hendriksen, Low temperature processed MnCo₂O₄ and MnCo_{1.8}Fe_{0.2}O₄ as effective protective coatings for solid oxide fuel cell interconnects at 750C, *J. Power Sources* 336 (2016) 408–418, <https://doi.org/10.1016/j.jpowsour.2016.11.011>.
- [28] C. 22H, Material Data Sheet No. 4050 VDM ® Crofer 22 H Report, 2010.
- [29] I. Ritucci, R. Kiebach, B. Talic, L. Han, P. Zielke, P.V. Hendriksen, H.L. Frandsen, Improving the interface adherence at sealings in solid oxide cell stacks, *J. Mater. Res.* (2019) 1–12, <https://doi.org/10.1557/jmr.2018.459>.
- [30] H.L. Frandsen, P.V. Hendriksen, B.S. Johansen, A Testing Apparatus and a Method of Operating the Same, IPC No. G01N3/18; G01N3/20. (Patent No. WO2014195304.), 2014.
- [31] P.G. Charalambides, H.C. Cao, J. Lund, A.G. Evans, Development of a test method for measuring the mixed mode fracture resistance of bimaterial interfaces, *Mech. Mater.* 8 (1990) 269–283, [https://doi.org/10.1016/0167-6636\(90\)90047-J](https://doi.org/10.1016/0167-6636(90)90047-J).
- [32] I. Hofinger, M. Oechsner, H.-A. Bahr, M.V. Swain, Modified four-point bending specimen for determining the interface fracture energy for thin, brittle layers, *Int. J. Fract. Mech.* 92 (1998) 213–220, <https://doi.org/10.1023/A:1007530932726>.
- [33] H.L. Frandsen, D.J. Curran, S. Rasmussen, P.V. Hendriksen, High throughput measurement of high temperature strength of ceramics in controlled atmosphere and its use on solid oxide fuel cell anode supports, *J. Power Sources* 258 (2014) 195–203, <https://doi.org/10.1016/j.jpowsour.2014.02.036>.
- [34] P.G. Charalambides, J. Lund, A.G. Evans, R.M. McMeeking, A test specimen for determining the fracture resistance of bimaterial interfaces, *J. Appl. Mech.* 56 (1989) 77, <https://doi.org/10.1115/1.3176069>.
- [35] M.C. Tucker, L.C. DeJonghe, V. Garcia-Negron, R. Trejo, E. Lara-Curzio, Mechanical and electrochemical performance of composite cathode contact materials for solid oxide fuel cells, *J. Power Sources* 239 (2013) 315–320, <https://doi.org/10.1016/j.jpowsour.2013.03.130>.
- [36] B. Talic, I. Ritucci, R. Kiebach, H.L. Frandsen, Improved robustness and a low area specific resistance with novel contact layers for the solid oxide cell air electrode, *ECS Trans.* (2019).
- [37] J. Malzbender, R.W. Steinbrech, L. Singheiser, Determination of the interfacial fracture energies of cathodes and glass ceramic sealants in a planar solid-oxide fuel cell design, *J. Mater. Res.* 18 (2003) 929–934, <https://doi.org/10.1557/JMR.2003.0127>.
- [38] W.N. Liu, X. Sun, E. Stephens, M.A. Khaleel, Life prediction of coated and uncoated metallic interconnect for solid oxide fuel cell applications, *J. Power Sources* 189 (2009) 1044–1050, <https://doi.org/10.1016/j.jpowsour.2008.12.143>.
- [39] M. Bobruk, S. Molin, M. Chen, T. Brylewski, P.V. Hendriksen, Sintering of MnCo₂O₄ coatings prepared by electrophoretic deposition, *Mater. Lett.* 213 (2018) 394–398, <https://doi.org/10.1016/j.matlet.2017.12.046>.
- [40] J.W. Stevenson, Z.G. Yang, G.G. Xia, Z. Nie, J.D. Templeton, Long-term oxidation behavior of spinel-coated ferritic stainless steel for solid oxide fuel cell interconnect applications, *J. Power Sources* 231 (2013) 256–263, <https://doi.org/10.1016/j.jpowsour.2013.01.033>.
- [41] J.A. Crawford, R.w. Vest, Electrical conductivity of single-crystal Cr₂O₃, *Rev. Mod. Phys.* 3 (1931) 156–189, <https://doi.org/10.1103/RevModPhys.3.156>.
- [42] A. Holt, P. Kofstad, Electrical conductivity and defect structure of Cr₂O₃. II. Reduced temperatures (<–1000°C), *Solid State Ion.* 69 (1994) 137–143, [https://doi.org/10.1016/0167-2738\(94\)90402-2](https://doi.org/10.1016/0167-2738(94)90402-2).
- [43] S. Molin, P. Jasinski, L. Mikkelsen, W. Zhang, M. Chen, P.V. Hendriksen, Modify, *J. Power Sources* 336 (2016) 408–418, <https://doi.org/10.1016/j.jpowsour.2016.11.011>.
- [44] B. Talic, I. Ritucci, R. Kiebach, P.V. Hendriksen, H.L. Frandsen, Improved robustness and low area specific resistance with novel contact layers for the solid oxide cell air electrode, *ECS Trans.* 91 (2019) 2225–2232, <https://doi.org/10.1149/09101.2225ecst>.
- [45] B. Talic, S. Molin, K. Wiik, P.V. Hendriksen, H.L. Lein, Comparison of iron and copper doped manganese cobalt spinel oxides as protective coatings for solid oxide fuel cell interconnects, *J. Power Sources* 372 (2017) 145–156, <https://doi.org/10.1016/j.jpowsour.2017.10.060>.
- [46] S. Koch, P.V. Hendriksen, Contact resistance at ceramic interfaces and its dependence on mechanical load, *Solid State Ion.* 168 (2004) 1–11, <https://doi.org/10.1016/j.ssi.2004.01.010>.
- [47] J.G. Grolig, J. Froitzheim, J.E. Svensson, Coated stainless steel 441 as interconnect material for solid oxide fuel cells: evolution of electrical properties, *J. Power Sources* 284 (2015) 321–327, <https://doi.org/10.1016/j.jpowsour.2015.03.029>.
- [48] J. Tallgren, O. Himanen, M. Bianco, J. Mikkola, O. Thomann, M. Rautanen, J. Kiviahio, J. Van herle, Method to measure area specific resistance and chromium migration simultaneously from solid oxide fuel cell interconnect materials, *Fuel Cells* 19 (2019) 570–577, <https://doi.org/10.1002/fuce.201800169>.